
Article:
Haque, MJ, Molla, MM, Khan, MAI orcid.org/0000-0002-7521-5458 et al. (1 more author) (2020) Graphics process unit accelerated lattice Boltzmann simulation of indoor air flow: Effects of sub-grid scale model in large-eddy simulation. Proceedings of the Institution of Mechanical Engineers, Part C: Journal of Mechanical Engineering Science, 234 (20). pp. 4024-4040. ISSN 0954-4062

https://doi.org/10.1177/0954406220919780

GPU Accelerated Lattice Boltzmann Simulation of Indoor Air flow: Effects of Subgrid-scale Model in Large-eddy Simulation

Md. Jahidul Haque[a], Md. Mamun Molla[b1], Md. Amirul Islam Khan [c], Kamrul Ahsan [d]

[a,b] *Department of Mathematics & Physics, North South University, Dhaka, 1229, Bangladesh.*
[b] *Center for Applied Scientific Computing (CASC), North South University, Dhaka, 1229, Bangladesh*
[c] *School of Civil Engineering, University of Leeds, Leeds LS2 9JT, UK*
[d] *SWECO UK Limited, Engineering, Environment and Design Consultancy, City Park 368 Alexandra Parade Glasgow, G31 3AU, UK*

Abstract

In this present study, three-dimensional (3D) lattice Boltzmann method (LBM) is implemented with the popular turbulence modeling method large-eddy simulation (LES) incorporating three different non-dynamic subgrid-scale (SGS) models Smagorinsky, Vreman and Wall-Adapting Local Eddy-viscosity (WALE) for finding the inhomogeneous turbulent airflow patterns inside a model room with a partition. The LES-LBM code is validated with the experimental results of Posner's model, where the model room having one partition at the bottom, one inlet, an outlet placed at top wall considered for the comparisons. The LBM code is also validated without any SGS model with the results of lid-driven flow in a cubic cavity. The present numerical simulations are performed by the graphics process unit (GPU) accelerated parallel programs using compute unified device architecture (CUDA) C platform. Double precession capable a Tesla k40 with 2880 CUDA cores NVIDIA GPU card has been used for these simulations. Graphics processor units have gained popularity in recent years as a propitious platform for numerical simulation of fluid dynamics. In fact, faster computational task performance in GPUs is one of the key factors for researchers to choose GPUs over conventional CPUs for the implementation of data-intensive numerical methods like LBM. The effects of the SGS model have been evaluated in terms of the mean velocity profiles, streamlines as well as turbulence characteristics and found that there are significant differences in the results due to the different SGS models.

Keywords: *GPU parallel computing; natural ventilation; turbulent air flow; lattice Boltzmann method; large-eddy simulation; subgrid-scale model*

1. Introduction

Natural ventilation for adequate indoor air flow has become a very important strategy in recent decades to reduce energy consumption due to mechanical heating, ventilation and air conditioning (HVAC) systems as well as maintaining good indoor air quality (IAQ). Since simulation of indoor air flow pattern is pivotal to the healthy environment, different accurate experimental research and computer simulations have got notable attractions in recent years. Hence, experimental tests for finding the suitable geometry to ensure adequate natural air supply are very expensive, numerical simulations of airflow patterns on various building design patterns have become popular in this decade. Numerical models are capable of detecting both laminar and

[1]Corresponding author (M. M. Molla)
Tel: +880255668200, Ext.1519, Fax: +880255668202.
Email: mamun.molla@northsouth.edu

turbulent flows inside any geometries with different obstacles. However, turbulent flows are very much identical to the real-world airflow phenomena, and different numerical turbulence models became popular for capturing detail turbulent behavior of airflow inside indoor environments.

In modern building design, different HAVC systems and natural ventilation strategies are applied where IAQ is the major concern to achieve good indoor environment. In this purpose, investigations on airflow patterns are the most crucial factors in IAQ research. Nowadays, natural ventilation (NV) strategies are more energy and cost efficient than the most of the mechanical ventilation methods. Experimental and numerical studies are improving NV strategies to create optimized geometries for enough airflow to maintain a pleasant indoor environment. In fact, NV strategies have been studied over this decade as such as the displacement ventilation by Xing et al. [1] and Mundt [2] showed the experimental results for displacement ventilation wheres Karimipanah and Awbi [3] proposed a impinging jet ventilation (IJV) where the authors compared results with the displacement ventilation methods to ensure improved air quality and showed improved indoor environment using IJV strategy . Even some personalized ventilation methods proposed by Shao and Li [4], Melikov [5] and Kaczmarczy et al. [6] were able to ensure non-uniform air distribution with the aid of the occupants who are not satisfied with uniform air distribution methods. But, most importantly, good NV strategies are being developed by the researchers with the help of many experimental and numerical studies over this decade. However, experimental studies like the researches of Rey and Velasco [7] and Jiang and Wang [8] on indoor airflow required huge cost and time although such studies delivered accurate results of ventilation models regarding different airflow parameters like air velocity, temperature, contaminated concentrations and relative humidity, etc. Furthermore, computational fluid dynamics (CFD) has been evolved as an efficient method without any practical experiment by measuring the specified geometries where the airflow parameters of a ventilation strategy are solved by the numerical solution. Visualizing fluid flow phenomena by solving the Navier-Stokes (N-S) equation is the most traditional CFD technique among the researchers alongside the lattice Boltzmann Method (LBM) of fluid flow. In fact, different CFD modeling in indoor environment under various geometries were developed by Wang et al. [9], Zhang and Chen [10] and Zhao et al. [11] while LBM implementation in IAQ domain was discussed in several works [12, 13, 14]. Specifically, Tian et al. [15] described a simulation using realizable k-ϵ model combined with a Lagrangian particle tracking model in three different geometries to find out indoor airflow and contaminant particle transportation.

In recent years, LBM become prominent in many engineering applications such as fluid flow and heat transfer simulation [16, 17], acoustics by Keating et al. [18], multiphase flows by Lee and Lin [19] and phase-change heat transfer [20]. Usually, traditional CFD models numerically solve discretized N-S equations to study fluid flow while non-conventional CFD models use LBM methods for finding fluid flow patterns. LBM uses more simplified approach than the N-S equations by relating pressure fields with the density of the fluid without taking consideration of solving computationally costly Poisson equation [21]. Moreover, at the beginning of finding a mathematically simplified fluid flow solver among the researchers, LBM was derived from the theory of lattice gas automata for recovering Navier-Stokes equation by Frisch et al. [22]. Later, the lattice Gas cellular automata (LGCA) model extended and improved by several researchers like [23, 24]. Notably, Wolf-Gladrow [25] recovered Naiver-Stokes equation using Chapman-Enskog expansion. Furthermore, LBM model is considered to be an efficient simulation model for direct numerical simulation (DNS) by disregarding the relation between the stress tensor and main strain tensor [26]. Besides, LBM is easy to implement for parallel computation to solve continuous fluid flow characteristics which were noted in the literature [21]. Also, the time complexity of the different simulation models based on LBE is better than the most of the traditional CFD models where N-S Equation are solved for simulating fluid flows. However, according to work of Si and Shi [26], the standard single-relaxation-time (SRT) LBM has

several disadvantages as such as it's numerical instability for simulating high Reynolds number flows if unresolved small-scale effects on large-scale dynamics are not considered as like DNS. Such disadvantages can be filtered through turbulence models like LES and Raynolds-averaged Navier-Stokes (RANS), hybrid RANS-LES, etc. along with various SGS modeling approaches for small-scale effect modeling.

Direct numerical simulation is the most accurate method to study turbulence of fluid flow although the time required for getting the result is very expensive and Pope [27] explained the effectiveness of DNS where it numerically resolves all eddies in turbulent fluid flow using comparatively larger grid computation. In consequence, RANS and LES have become popular in recent years to reduce the time and grid required in DNS to simulate the fluid flow phenomena. RANS approach includes modeling of Reynolds stress generating from time-averaged turbulent velocity fluctuations using different CFD models such as standard $k-\epsilon$ model presented in Shih et al. [28], the RNG $k-\epsilon$ model showed in [29] and $k-\omega$ model discussed in [30]. For this reason, RANS approach always solves mean results of fluid characteristics within the flow domain. Thus, RANS modeling is suitable for finding steady flow structure in low and large Reynolds number while the method fails to capture small turbulence scales of unsteady turbulence region of the fluid flow which was observed by Lakehal and Rodi [31]. On the other hand, LES presented in [32] is an intermediate approach between RANS and DNS where small sub-grid scales are modeled, and large scales are numerically resolved.

LES had been used in turbulence studies of many real-world scenarios like indoor airflow simulation by Zhang and Chen [33], wind gusts [34] and turbulent square jet flow [35]. After filtering the turbulent flow into small and large eddies, various CFD methods discussed in [35, 36], were used to solve LES filtered equations, and the terms are associating small eddies in the turbulent structure are modeled using different Sub-grid scale (SGS) models showed in [37]. The SGS model was first proposed by Smagorinsky [38] commonly known as Smagorinsky model, Vreman model illustrated in the literature of Vreman [39], the WALE model discussed in [40, 41],and the Dynamic SGS model by Germano et al. [42] and Lilly [43]. In evident, Emmerich et al. [44] applied Fast Fourier Transform (FFT)-based Poisson solver with Smagorinsky model to simulate the transport of smoke and hot gases during a fire in an enclosure. Recently, Sajjadi et al. [45] used a multiple-relaxation-time (MRT)-LBM-LES method with the shear-improved Smagorinsky model to simulate the airflow inside a room. Wang and Chen [46] developed a hybrid RANS-LES method to simulate indoor airflow where near wall region turbulence is modeled through N-S based RANS approach, and subgrid scale turbulence is captured using LES method. However, standard Smagorinsky SGS model has few disadvantages like less accuracy in the inhomogeneous flow field and producing virtual eddy viscosity in wall-bounded geometries. In evident, Vreman [39] developed a new approach rather than Smagorinsky model to calculate more accurate results of eddy viscosity for inhomogeneous flow field. Furthermore, Moghadam et al. [40] implemented a wall adapted local eddy viscosity LES (LES-WALE) SGS model for simulating turbulence around a circular cylinder to reduce the impact of damping factor of Smagorinsky SGS models. Although there are many researches in the literature available regarding the simulation of airflow patterns, there are not many comparative studies on the turbulent effects of different SGS model within the indoor environment domain. Besides, most of the LES rendered SGS models are based on traditional CFD techniques although there are very few litterateurs available that studied multiple SGS models using LBM framework. Moreover, many of these LBM-LES or N-S based LES requires intensive computational resources such as cluster computers or supercomputers as well as parallel code writing platforms like Message Passing Interface (MPI) or OpenMP for simulating detailed airflow pattern. Due to resource shortage, these methods often seems to be bit difficult to implement in a handful time line. In recent years, General Purpose Graphics Processor Units(GPGPU) become popular for performing scientific computations in many engineering ap-

plications including LBM in indoor airflow simulation due to the low cost and parallel compute capability of GPU.

Graphics processor units have the hardware architecture that requires parallel computation while lattice Boltzmann method has massively parallel computational capability in complex geometries where related works found in the literature [47, 48, 16, 49]. Generally, LBM uses uniform grid generation for lattice nodes where information of nearest neighbor nodes is being updated in each time step. This uniform grid generation restricts the collisions of lattice node among the updated neighbor nodes during fluid flow simulation. Bernaschi et al. [50] introduced GPU computing for multi-physics, multi-scale simulations of particles embedded and interacting with fluids where LBM is used for solving the hydro-kinetic representation of the fluid. Also, Bailey et al. [51] simulated LBM method in the context of $D3Q19$ lattice model where GPU computation increased the performance of the simulation over 28 times than CPU computing based on quad-core CPU using OpenMP. Later, Delbosc et al. [52] applied an LBM based interactive and real-time simulation program to evaluate the suitability, accuracy, and usefulness of a $3D$ real-time, thermal and turbulent air flow solver running on a GPU platform. Furthermore, Obrecht et al. [53] proposed a 3D MRT-LBM method which achieved 86% of the effective maximum throughput of global memory during the implementation of the program. However, there have been not much research on different SGS model implementation using GPU computing for indoor airflow simulation.

In our present study, we implemented lattice Boltzmann method in conjunction with large eddy simulation for three different SGS models Smagorinsky, Vreman, and WALE in GPU computing platform using NVIDIA's Compute Unified Device Architecture (CUDA) C programming language for indoor airflow simulation. All three LBM-LES-SGS models are validated with experimental data of earlier research considering a model hospital room with one partition and having inlet and outlet in the top wall while $Re = 1600$. For the present study, $Re = 5000$ is considered to evaluate the effects of SGS model on the large scale and small scale turbulent flow characteristics. Molla et al. [54] studied the inhomogeneous turbulent flow simulation using the linear and non-linear dynamics SGS models for the Navier-Stokes equations and found significant effects of the SGS models on the flow simulation.

2. Mathematical Formulations for Airflow Simulation

2.1. Lattice Boltzmann Method (LBM)

LBM is an efficient computational fluid dynamics(CFD) technique for solving airflow patterns in the indoor environment. LBM is originated from the concept of lattice gas cellular automata where each unique cell is discretized regarding position state and achieves new states in each time step using a rule of distribution among neighbor cells. In LBM, macroscopic scale continuity of fluid is solved by assuming fluid particles as lattice nodes through two major event: the collision where fluid particles are discretized in terms of space and collide with each other to achieve an equilibrium state in a constant time and the streaming (distribution of new states among particles) in context of a set of discrete trajectories. LBM method is solved in terms of lattice model while different 3D models as D3Q13, D3Q15, D3Q19, and D3Q27 model for solving fluid flow phenomena in any physical geometry. In the 3D lattice Boltzmann method, the D3Q19 lattice model is the most popular lattice model to implement the LBM algorithm since it is giving accurate results comparing with the results obtained from the Navier-Stokes equation. The D3Q19 model has 19 discrete velocities which state directions and positions of the different lattices. In this paper, D3Q19 lattice model is used to implement flow simulation in LBM which is illustrated in Figure 1.

The discretized LBM equation for particle distribution as described in [55] can be written as follows:

$$f_i\left(\mathbf{x}+\mathbf{e_i}\Delta t, t+\Delta t\right) = f_i\left(\mathbf{x},t\right) - \frac{1}{\tau}\left[f_i\left(\mathbf{x},t\right) - f_i^{eq}\left(\mathbf{x},t\right)\right] \tag{1}$$

where f_i and f_i^{eq} is denoted as density distribution function and local equilibrium density distribution function of the the fluid in position $\mathbf{x}$ at time t where i is the discrete position of the lattice model. Here τ is the relaxation time which is defined in Eqn.(2) where ν_0 is the molecular kinematic viscosity of the fluid and c_s is the speed of sound which is related to the lattice speed $c \stackrel{\text{def}}{=} \frac{\Delta x}{\Delta t} = 1$ where $c_s \stackrel{\text{def}}{=} \frac{c}{\sqrt{3}}$.

$$\tau = \frac{1}{2} + \frac{\nu_0}{c_s^2 \Delta t} \tag{2}$$

In every discrete time step, each density distribution changes due to the propagation of fluid particles and reaches its equilibrium. The local equilibrium of the lattice nodes which is illustrated in Eqn.(3) depends on the weight coefficient w_i, discrete velocities $\mathbf{e_i}$ and velocity vector $\mathbf{u}$ for each position of the lattice model.

$$f_i^{eq}\left(\mathbf{x},t\right) = \rho w_i \left[1 + 3\frac{\mathbf{e_i}\cdot\mathbf{u}}{c^2} + \frac{9}{2}\frac{\left(\mathbf{e_i}\cdot\mathbf{u}\right)^2}{c^4} - \frac{3}{2}\frac{\mathbf{u}^2}{c^2}\right] \tag{3}$$

The weight coefficient w_i and $\mathbf{e_i}$ velocities for each lattice positions are defined as follows:

$$\mathrm{w}_i = \begin{cases} \frac{1}{3} & i = 0 \\ \frac{1}{18} & i = 1-6 \\ \frac{1}{36} & i = 7-18 \end{cases} \qquad \mathbf{e_i} = \begin{cases} (0,0,0) & i = 0 \\ (\pm 1,0,0),(0,\pm 1,0),(0,0,\pm 1) & i = 1-6 \\ (\pm 1,\pm 1,0),(\pm 1,0,\pm 1),(0,\pm 1,\pm 1) & i = 7-18 \end{cases}$$

Distribution functions f_i and f_i^{eq} defined in Eqn.(2) and Eqn.(3) are updated after the collision and streaming step for each lattice node in each time steps. After that the macroscopic fluid density and fluid velocity is calculated by considering particle distribution function f_i and particle velocity $\mathbf{e_i}$ using the equations are given bellow:

$$\rho = \sum_{i=0}^{18} f_i \tag{4}$$

$$\rho\mathbf{u} = \sum_{i=0}^{18} \mathbf{e_i} f_i \tag{5}$$

3. Large Eddy Simulation in LBM

Turbulent airflow describes the real scenario of the indoor environment which occurs due to shear stress generated in high Reynolds number Re within the flow field. Since dynamic small-scale motions are not considered in calculating the kinematic viscosity of the fluid in LBM, numerical instability occurs at high Reynolds numbers. Extended formulation of the formal LBM equations with LES is the possible solution for capturing small-scale microscopic flow continuity to achieve numerical stability of the fluid simulation. Turbulent flow in the fluid region is determined by the effect of eddy viscosity of the fluid. For this reason, LES decomposes the viscosity of the fluid into molecular viscosity (ν_0) obtained from the Reynolds number and the turbulent eddy viscosity $\nu_t(\mathbf{x},t)$ is calculated by using different sub-grid scale models. The total viscosity of the fluid becomes as follows:

$$\nu_{total}(\mathbf{x},t) = \nu_0 + \nu_t(\mathbf{x},t) \tag{6}$$

$$\tau_{total}(\mathbf{x},t) = \tau_0 + \tau_t(\mathbf{x},t) \tag{7}$$

$$\tau_t(\mathbf{x},t) = \frac{1}{2} + \frac{1}{3}\nu_t(\mathbf{x},t) \tag{8}$$

Thus, the total relaxation-time for LES can be written as:

$$\tau_{total} = \frac{1}{2} + \frac{1}{3}\nu_{total}(\mathbf{x},t) \tag{9}$$

Large eddy simulation produces enough turbulent flow phenomena comparing to different RANS approaches. The airflow patterns in a geometry get turbulent at high Reynolds numbers, and the turbulence creates numerical instability within the numerical method. Specifically, small energy dissipation from the smallest Kolmogorov scales (small subgrid eddies) creates this turbulence in the flow simulation. Although DNS is capable of capturing smallest eddies of this turbulent flow in the finer mesh of a big grid by maintaining numerical stability, LES is also capable of capturing small subgrid-scales even smaller grid size through modeling the turbulent behavior of the flow using SGS models. Moreover, the contribution of turbulent flow structures within the total flow phenomena partially depends on the subgrid-scale dissipation constant. In fact, the subgrid-scale contribution can be increased with the increment of SGS constant to achieve more stable flow phenomena which provides more modeling of turbulent flows rather than solving it.

The eddy viscosity can be calculated by different SGS models to model the unresolved small-scale eddies of turbulent flow. In this paper, three SGS models are used separately for finding the eddy viscosity of the fluid, such as: (i) Smagornisky model [38], (ii) Vreman model [39] and (iii) WALE model [40].

3.1. Smagorinsky SGS Model (SM)

Smagorinsky model is the most widely used sub-grid scale model for the simulation fluid which was first proposed by [38]. For capturing the sub-grid scale motion the eddy viscosity ν_t of Samgronisky model is as follows:

$$\nu_t(\mathbf{x},t) = C_s\Delta^2|S| \tag{10}$$

where Δ is the filter width, $C_s$is the Samgronisky constant and $|S|$ is the magnitude of local strain tensor of the fluid which can be computed using Frobenius norm that used in [52] as follows:

$$|S| = \sqrt{2S_{\alpha\beta}S_{\alpha\beta}} \tag{11}$$

Here, the local strain tensor $S_{\alpha\beta}$ is computed as:

$$S_{\alpha\beta} = \frac{1}{2}\left(\frac{\partial u_\alpha}{\partial x_\beta} + \frac{\partial u_\beta}{\partial x_\alpha}\right) \tag{12}$$

However, in LBM $S_{\alpha\beta}$ can be computed using non-equilibrium stress tensor $\Pi_{\alpha\beta}$ in Eqn.(14) and the calculation of $S_{\alpha\beta}$ according to the following formula as in [52].

$$|S| = \frac{1}{6C_s\Delta^2}\left(\sqrt{{\nu_0}^2 + 18C_s^2\Delta^2\sqrt{\Pi_{\alpha\beta}\Pi_{\alpha\beta}}} - \nu_0\right) \tag{13}$$

$$\Pi_{\alpha\beta} = \sum_{i=0}^{18} e_{i\alpha} e_{j\beta} \left(f_i - f_i^{eq}\right) \tag{14}$$

Here α and β are iterated through three spatial dimensions. Moreover, the calculated local strain rate tensor is very crucial in capturing the subgrid-scale motion in the turbulent fluid region. However, Vreman [39] showed that the SGS model constant (C_s) in Eqn.(10) is not a universal constant for Smagorinsky model so that the model produce inaccurate results for inhomogeneous flow in the transitional region of the fluid in higher C_s values.

3.2. Vreman SGS model (VM)

To remove the limitations of Smagorinsky SGS model, vreman [39] developed another SGS model that is known as Verman SGS model. In VM, alternative approach is considered where a (3×3) derivative matrix of velocity vector $\mathbf{u}$ is calculated as α_{ij} and the local strain tensor β_{ij} is calculated from α_{ij}. Then the subgrid dissipation is calculated by the B_β and the turbulent eddy viscosity as in [39] is calculated as follows :

$$\nu_t(\mathbf{x}, t) = C_v \sqrt{\frac{B_\beta}{\alpha_{ij}.\alpha_{ij}}} \tag{15}$$

$$\alpha_{ij} = \frac{\partial u_j}{\partial x_i} \tag{16}$$

$$\beta_{ij} = \Delta^2 \alpha_{mi} \alpha_{mj} \tag{17}$$

$$B_\beta = \beta_{11}\beta_{12} - \beta_{12}^2 + \beta_{11}\beta_{33} - \beta_{13}^2 + \beta_{22}\beta_{33} - \beta_{23}^2 \tag{18}$$

Here C_v is the SGS model constant which is related to the Smagorinsky constant C_s where $C_v \approx 2.5 C_s^2$ was defined by [39].

3.3. WALE SGS model (WM)

In standard Smagorinsky SGS model (SM), turbulent behavior is assumed by non-zero magnitude at the wall boundary of the geometry as soon as velocity gradient exists although the eddy viscosity should be zero at the wall due no turbulence [41]. To remove this limitation of SM, wall adapted local SGS model WALE (WM) was used in several studies [56, 40]. Therefore, WM is an another alternative approach considering the symmetric part of the square of the gradient velocity tensor g_{ij} is defined as $g_{ij} \stackrel{\text{def}}{=} \frac{\partial u_i}{\partial x_i}$. A new operator ${S^d}_{ij}$ is calculated for treating the wall behavior as follows:

$${S^d}_{ij} = \frac{1}{2}\left({g_{ij}}^2 + {g_{ji}}^2\right) - \frac{1}{3}\delta_{ij}{g_{kk}}^2 \tag{19}$$

where δ_{ij} is the Kronecker delta. The local strain tensor S_{ij} in WM is unlike the tensor $S_{\alpha\beta}$ of SM in Eqn.(12). The eddy viscosity of WM is defined as follows:

$$\nu_t(\mathbf{x}, t) = (C_w \Delta)^2 \frac{\left({S^d}_{ij} {S^d}_{ij}\right)^{\frac{3}{2}}}{\left(S_{ij}S_{ij}\right)^{\frac{5}{2}} + \left({S^d}_{ij}{S^d}_{ij}\right)^{\frac{5}{4}}} \tag{20}$$

In the WM, generally the WM constant is used as $C_w = 0.5$. According to the literature [41], the SGS constant of the model can be related to the Standard Smagorinsky model constant where C_w can be interpreted as $0.55 \leq C_w \leq 0.60$ which is equivalent as $C_s = 0.18$.

3.4. Boundary Conditions

In 3D physical geometry, boundary conditions have been imposed for studying airflow near six surface wall illustrated in a lattice model of Figure 1. For the model geometry is shown in Figure 4, well known bounce-back conditions are applied to the walls having no inlet or outlet and unknown post-streaming density distribution functions are calculated in Eqn.(21) at the inlet of the top wall using the formula suggested by Ladd [57]. The zero gradient rule has been applied at the outlet for calculating post streaming values in Eqn.(22). The boundary conditions for the inlet and the outlet at the top wall are as follows:

$$f_{\bar{i}}\left(\mathbf{x}, t+\Delta t\right) = f_i\left(\mathbf{x}, t\right) - 6\rho_w w_i \mathbf{u_w} \cdot \mathbf{e_i} \tag{21}$$

$$f_i\left(\mathbf{x_b}, t+\Delta t\right) = f_i\left(\mathbf{x_f}, t+\Delta t\right) \tag{22}$$

Here $\mathbf{u_w}$ is the inlet velocity, $\mathbf{x_b}$ is the boundary node and $\mathbf{x_f}$ is the inner fluid node.

3.5. Implementation of the LBM-LES based SGS Model using CUDA C

Lattice Boltzmann method is a data-intensive method because of the solving of all distribution functions as well as the streaming and collision events. The LBM-LES framework in this present study is used three sub-grid scale (SGS) models Smagorinsky, Vreman and WALE for the simulation of turbulent behaviors of airflow patterns inside an indoor geometry. The algorithm for the LBM-LES-SM simulation is given below:

LBM-LES ALGORITHM

begin
GLOBAL initialization:
SET lattice configuration
SET geometric configuration
Main Program start:
device variable allocation for density distribution (f_i), equilibrium distribution ($f_i^{equilibrium}$)
host variable allocation
initial kernel call
SET time=currentTime()
while(TIME<TIMESETPS)
do collision-streaming-kernel
device to host memory transfer
visualize the result
initial kernel::
SET f_i for $D3Q19$ lattice
SET $u_x = 0$, $u_y = 0$, $u_z = 0$
collision-streaming-kernel (Using pull-out scheme)::
SET $f_i^{equilibrium}$ for D3Q19 lattice
GET ν_{sgs} for the SGS model
GET f_i^{post} from $\nu_t = \nu + \nu_{sgs}$
SET f_i=f_i^{post} (f_i^{post} is the array of post collision values)
apply boundary conditions
UPDATE ρ, u_x, u_y and u_z
UPDATE end time loop

3.6. Optimizations of the LBM-LES based SGS Model

The parallel program in GPU can be computationally inefficient in case of unaligned memory accessing patterns and unnecessary global memory usage used by the DRAM of the GPU. In GPU based simulation, minimization of global memory usage and efficient memory accessing patterns are very crucial to achieve good computational performance. For ensuring the efficient use of parallel architecture of GPU, we used Structure of Array(SOA) data to use the distribution function $f_i[i + jD_i + kD_iD_j]$ rather than using array of structure(AOS) while detailed comparisons of the these data structures is found in the literature [52]. Moreover, CUDA device to host or host to devise operation is a costly in CUDA programming due to the memory latency issues of the GPU hardware. To hide the memory latency, GPU occupies all the processor cores for instruction processing to give DRAM enough time for performing data transactions. Therefore, memory usage of the DRAM of the hardware is minimized by using the single kernel of collision and streaming of the particle for a minimal number of host to device data transfer. However, the LES-LBM program has critical performance issues at the time of computing post-collision values due to misaligned memory addressing in GPU. To improve the simulation performance we have used two different memory accessing patterns in GPU: the pull-in and pull-out collision-streaming-kernel. The pull-out LES-LBM kernel is presented below:

PULL-OUT LBM-LES KERNEL for Smagorinsky SGS model

SET $f_i^{equilibrium}$ from u_x, u_y and u_z of previous time-step (Coalesced memory read)
GET for the non-equilibrium stress tensor from f_i
GET ν_{sgs} for the SGS model
GET f_i^{post} from ν as post collision values
SET f_i=f_i^{post} as streaming of particles (no coalescing memory write)
apply boundary conditions
UPDATE ρ, u_x, u_y and u_z

The collision between particles is preferred over streaming between them in the above kernel of PULL-OUT LBM-LES. Since the velocities of the previously computed node of lattice A in Figure2 are used to achieve the relaxed f_i^{post} in a single lattice node the aligned access of the memory read is achieved while unaligned memory write is occurred due to storing the f_i from the f_i^{post} which can be streamed to the adjacent nodes of Lattice B. This memory addressing scheme led to unnecessary memory allocation in the GPU register memory, and that indicates the inefficient use of massively parallel architecture of GPU. On the other hand, the algorithm of pull-in scheme is demonstrated below:

PULL-IN LBM-LES KERNEL for Smagorinsky SGS model

SET f_i=f_i^{post} from the values of previous time step as streaming of particles (Coalesced memory write)
apply boundary conditions
UPDATE ρ, u_x, u_y and u_z
SET $f_i^{equilibrium}$ from u_x, u_y and u_z of current time-step (no coalescing in memory read)
GET for the non-equilibrium stress tensor
GET ν_{sgs} for the SGS model
GET f_i^{post} from ν as post collision values

In PULL-IN LES-LBM, the all-new f_i for Lattice node A of Figure 3 are stored in the memory of the GPU registers from aligned post-collision values of f_i^{post} found in previous time step. Due to this aligned memory write, the f_i^{post} values of the current time-step is computed after achieving the local equilibrium by reading the misaligned values of velocity distributions form the neighboring nodes of Lattice B. In our simulation program on NVIDIA Tesla k40, the PULL-IN LES-LBM scheme has 7.32% computational time efficiency rather than the PULL-OUT LES-LBM scheme. Delbosc et al. [52] achieved similar improvement of 6% performance on choosing aligned memory write (PULL-IN) over aligned memory read (PULL-OUT) which was referred as a push-out method for coalesced memory write implemented on NVIDIA Tesla c2070.

Although the optimization in GPU code can be achieved through proper use of global memory and efficient pull-in scheme within the LES-LBM algorithm, shared memory can be used to improve the efficiency of current pull-in based LBM implementations discussed in [58, 53].

4. Results and Discussion

In our present study, we implemented lattice Boltzmann method in conjunction with large eddy simulation for three different SGS models Smagorinsky, Vreman, and WALE in GPU computing platform using NVIDIA's CUDA C programming language for indoor airflow simulation. The all three LES-LBM SGS models are validated with experimental data of earlier research considering a model hospital room with one partition as well as one inlet and outlet in the top wall while $Re = 1600$. For the present study, the effects of SGS model have been evaluating on the large scale and small flow characteristics the Reynolds number, $Re = 5000$ is considered.

4.1. Physical Geometry for the LES-LBM Simulation

The model room of Posner et al. [59] illustrated in Figure 4, is used for the validation of three SGS model. This room has one $l \times l = 0.101 \times .101$ m^2 square shaped inlet and outlet in the top wall and a partition having half-height $(H/2)$ of the room placed in the middle of the room. The room size is $(L \times W \times H) \approx (.914m \times .457m \times .305)$ while L, W and H are the length, width and height of the room respectively. The height of the room H is chosen for the reference length for the non-dimensionalization of lengths in all comparisons in the subsequent subsections. Hence, this validation case is also used in different indoor airflow related literature [59, 15], we conducted a detailed study of the turbulent airflow in the context of this geometry.

4.2. LBM Code Validation for the Lid-Driven Cubic Cavity with Re = 1000

Ensuring accurate numerical results of turbulent flow using the LES-LBM method, code validation is an essential step of any numerical research. At first, we have validated our implemented CUDA C LBM code for the well-known benchmark problem of fluid flow in a 3D lid-driven cubic cavity (Figure 5) without applying any SGS model to ensure that the main LBM code is correct. For this validation, the lattice size 256^3 is used as a uniform computational grid. The LBM results of lid-driven cubic cavity are compared with the numerical results of Shu et al. [60] and Ku et al. [61] while $Re \stackrel{\text{def}}{=} \frac{UH}{\nu_0} = 1000$, where H is the height of the cavity. Shu et al. [60] studied $3D$ Navier-Stokes (N-S) equation using differential quadrature (DQ) method and tested their computational model in the context of 3-D lid-driven cubic cavity while maximum $Re = 1000$. On the other hand, Ku et al. [61] solved 3D N-S equations using the pseudospectral method and showed comparisons of velocity profiles with previously studied available results. In our LBM study, we used $U = 0.1$ as lid velocity, and the results are compared for the horizontal u/U and vertical w/U velocity components at the mid plane of

the cavity. In the comparisons, Figure 6(a) shows the u/U velocity along the yz-plane of the geometry where Figure 6.(b) shows w/U along the xz-plane of the geometry. The comparison between present LBM results and available N-S results illustrated in Figure6 shows excellent agreement which establishes our LBM CUDA C code as a valid numerical tool. In the next subsection, we will implement LES-LBM with three different SGS models.

4.3. LES-LBM Code Validation for the Indoor Air Flow Simulation with $Re = 1600$

For the second stage of the code validation, our implemented LES-LBM code being tested with the experimental model of Posner et al. [59] (see Figure 4), since air flow simulation in this model room has been studied in some of the well-known numerical experiments of [45, 15] using traditional CFD techniques. [59] used this geometry (Figure 4) to measure airflow pattern by the Laser Doppler Anemometry (LDA) while they also validated their experimental results with RNG $k-\epsilon$ and standard $k-\epsilon$ RANS approach for $Re = 1600$. Moreover, [15] used a standard $k-\omega$ RANS approach for simulating airflow patterns of ventilated geometries with partition and they validated their work with the experimental data of [59].

To validate the present LES-LBM code with three different SGS models, the Reynolds number $Re \stackrel{\text{def}}{=} \frac{Ul}{\nu_0} = 1600$, where l is the length or width of the inlet, has been taken as like [59]. For stable LBM simulation, the inlet velocity $U = 0.1$m/s is used even though in experiment they used 0.25 m/s as inlet velocity. In LBM simulation l is the number of lattices for the inlet length or width and is calculates as $\frac{0.101}{0.914} \times N_x$, where N_x is the number of lattices in horizontal direction. In the case of implementing Smagorinsky, Vreman and WALE SGS models three different SGS constant values are applied where $C_s = 0.1$ for SM, $C_v = 2.5{C_s}^2$ for VM and for WM $C_w = 0.5$ and computational lattice size of $N_x \times N_y \times N_z \approx 260 \times 130 \times 88$ has been used to capture sub-grid scale effect of the turbulent airflow. The scenario is, when air enters the room with a velocity of U towards z-direction from the inlet and leaves the room through the outlet. For the comparison, the numerical results are presented in terms of the time-mean vertical velocity $\langle w \rangle$ at two different locations: (i) just above the partition (horizontal line parallel to x-axis) at $z/H = 0.51$ and $y/H = 0.5$ shown in Figure 7(a) and at (ii) bellow to the inlet (vertical line parallel to the z-axis) at $x/H = 2.61$ and $y/H = 0.5$ shown in Figure 7(b). Here it should be explained how the numerical results are compared with the experimental results. There are two ways to compare the present results with the experimental results: (i) the experimental results can be normalized by their inlet velocity 0.25 m/s and then compare with the non-dimensional (by $U = 0.1$ m/s) LBM results or (ii) the non-dimensional LBM results can be rescaled by the experimental inlet velocity 0.25m/s. In this study, the second procedure has been adopted for the comparison. From Figure 7(a), it is seen that the time-mean vertical velocity, $\langle w \rangle$, shows good agreement with experimental results of [59]. On the hand, the mean velocity, $\langle w \rangle$ of Figure 7(b) is slightly under predicted by the LBM than the experimental results. Moreover, qualitatively this comparison is quite similar among the literature of [45] and [15]. In this low Re, the distribution of the time-mean velocity shows little discrepancies for all three SGS models.

4.4. Grid Independence Test for $Re = 5000$

After validating code, the further investigation will be conducted for higher $Re = 5000$ to understand the effects of different SGS models in LES-LBM. A grid independence test for the Smagorinisky SGS models has been done considering five different grid arrangements, such as, (i)Case 1: $N_x \times N_y \times N_z \approx 60 \times 30 \times 20$, (ii)Case 2: $160 \times 80 \times 54$, (iii)Case 3: $260 \times 130 \times 88$, (iv)Case 4: $360 \times 180 \times 120$ and (v)Case 5: $460 \times 230 \times 154$. Grid independence results are shown in terms of the time-mean vertical velocity $\langle w \rangle / U$ in Figure 8(a) and turbulence kinetic energy (TKE) in Figure 8(b). considering $C_s = 0.2$. It is seen that individually for streamwise velocity and TKE, the results are almost same in Case 4 and 5 and here Case 4 is considered for the whole simulation.

4.5. Basic Flow Characteristics for $Re = 5000$

Basic airflow patterns are illustrated through the time-averaged velocity profiles using [59] model. In Figure 9, normalized time-averaged vertical velocity, $\langle w \rangle / U$ is shown when air flows along the x-direction of the flow above the partition at $(z/H = 0.51)$. A relatively higher Reynolds number $Re = 5000$ is used to compute the flow feature where velocity increment for all three SGS models is observed at partition region as well as near the wall of the room in which air is entering. In this case, air enters in the room at the inlet to the downward direction of the z axis at $x/H = 2.25$ position and all three SGS models have increasing negative $\langle w \rangle$ velocity while air approaches towards the bottom wall. In LES-VM with $C_v = 0.1 \left(C_v = 2.5{C_s}^2 \right)$ has the highest magnitude of $|\langle w \rangle|/U$ at the near wall region than LES-SM with $C_s = 0.2$ and LES-WM with $C_w = 0.60$. On the other hand, LES-WM has lower velocity magnitude than the other two LES models. It is a clear indication from the figure that the different SGS models play an important role in simulating turbulent flow features.

In Figure 10(a)-(c), the time-averaged velocity components $\langle u \rangle / U$ (normal to the wall), $\langle v \rangle / U$ (spanwise) and $\langle w \rangle / U$ (streamwise) are presented for the region below inlet jet along the vertical line at $x = 2.25H$. Since the flow developed towards the opposite direction of positive z-axis, the velocity components are increased towards the negative direction of z-axis at the inlet region and then gradually decreases as the flow approaches towards the bottom wall. In Figure 10(a), $\langle u \rangle / U$ is displayed where all three SGS models have almost identical velocity magnitudes while air distributes into the room from the top to the bottom wall. In Figure 10(b), $\langle v \rangle / U$ is shown where LES-SM has low-velocity magnitudes than the other two SGS models as air approaches towards the bottom wall after the increment of velocity until the air reaches at the middle of the room $z/H = 0.50$. In this case, LES-WM is over predicted, and LES-VM is under predicted than the LES-SM model. Figure 10(c) shows similar trends of the vertical velocity, $\langle w \rangle / U$ for all three models and has stable negative velocity magnitudes unlike $\langle u \rangle / U$ and $\langle v \rangle / U$ in Figure 10(a)-(b). In Figure 10(c), highest velocity magnitude is seen at $z/H = 0.3$, and then the velocity gets stable until the air reaches the bottom wall boundary. In LES-VM shows the higher velocity fluctuations than the Smagorinsky model. On the contrary, LES-WM is slightly under predicted than the other two subgrid models regarding mean $\langle w \rangle / U$ velocity.

Figure 11(a)-(c) depict the xz-plane contours of the non-dimensionalized streamlines appended on the vertical mean velocity field, $\langle w \rangle / U$ for three different SGS models while $Re = 5000$ at $y/H = 0.5$. The continuous air flow distribution is observed for all three models while air enters the room and circulates all over the room. The flow creates vortexes in the presence of obstacles like wall boundary or partition inside the room. In Figure 11 (a) the streamlines show a good visualization of boundary conditions applied to the partition walls as well as wall boundaries. The air flow gets weaker after flow collides with the partition walls and the turbulent air flow smoothly becomes transitional flow until it became laminar at near left boundary wall. In evident in the Figure 11(a) higher magnitudes of $\langle w \rangle / U$ are seen at the partition as well as right boundary wall. In Figure 11(b) LES-VM shows slightly different flow simulation as the mean velocity magnitudes of LES-VM are higher than LES-SM or LES-WM. In this figure, it is clear that this higher values of the vertical magnitudes create more vortexes than other two models while the flow faces obstacles that ensure more recirculation zones in the air distribution region. On the other hand, LES-WM has stable flow state that is similar to the results obtained form LES-SM.

4.6. Turbulent flow features for $Re = 5000$

In context of [59] experimental geometry with one partition, different turbulent flow features are discussed in this section. Turbulent airflow can be explained through the turbulent intensity and Reynolds stresses. The turbulent intensity in terms of root-mean-square (rms) velocity

fluctuations is calculated by $u_{rms} = \sqrt{\langle u'^2 \rangle}$, $v_{rms} = \sqrt{\langle v'^2 \rangle}$ and $w_{rms} = \sqrt{\langle w'^2 \rangle}$ and normalized by the inlet velocity U are displayed in Figure 12(a)-(c) respectively. Turbulent intensity increase as the flow develops due to the presence of different obstacles. In Figure 12(a), u_{rms} is depicted for the turbulence intensity for three SGS models where Vremen model has the highest turbulence intensity, and Smagorinsky model has the lower intensity. In Figure 12(b), v_{rms} for all the SGS models are almost identical when air enters the room through the inlet. It is clear in the figure that the turbulent strength gradually decreases with flow distribution to the whole room and slightly increased near the wall because of the shear stress generated at the wall. The maximum turbulent strengths are seen in Figure 12(c) for the normal stress component of vertical velocity (w_{rms}) where LES-VM shows the highest magnitude of $w_{rms} = 0.63$ and LES-WM has the lowest magnitude of $w_{rms} = 0.53$ at the inlet of the room.

Turbulent energy is extracted from the mean flow which can be defined as turbulent kinetic energy (TKE). These turbulent behaviors are seen due to the energy dissipation of both large scale and small scale eddies which are generated during the collision of air particles with different obstacles like partition or wall. Figure 13 illustrates the energy dissipation of all three models for the above partition region, the region below the inlet airflow and the near wall region. In Figure 13(a), the turbulent energy above the partition is shown where Vreman model has better energy dissipation, and WALE model has the lowest amount of energy resulting $TKE/U^2 = 0.33$, unlike the rms and Reynolds stress distribution. According to [41]work, rectification of the virtual eddy viscosity of the Smagorinsky model by the WALE model at the wall boundary, the overall magnitude of turbulence energy got lower than Smagoringky model which corrects the flow phenomena as no turbulence at wall boundary. In Figure 13(b) shows the energy dissipation where inlet jet airflow enters the room at horizontal position of $x/H = 2.25$. In this figure, LES-VM has higher TKE values than LES-SM and LES-WM have lower TKE values than LES-SM. Also, TKE spikes are seen simultaneously at the wall boundary after the collision of air particles due to the bounce back scheme. It is also observed identical energy dissipation graphs for all three SGS models near the wall boundary in Figure 13(c) where most turbulence occurs at the inlet and TKE gradually decreases as the flow is distributed through the whole room.

Figure 14 represents the contours of turbulent kinetic energy for LBM-LES-Smagorinsky, LBM-LES-Vreman, and LBM-LES-WALE where all models have nearly similar turbulent regions within the geometry. WALE model has good wall adapted energy dissipation in the Figure 14(c) rather than the Smagorinsky model shown in Figure 14(a). In general, LES-VM has better energy dissipation than the other two models with the highest magnitude of $TKE = 0.89$ shown in Figure 14(b). It is proved that different approaches of using SGS model for simulating turbulent behaviors impacted differently.

4.7. Sensitivity of different Sub Grid Scale Model Constants

Figure 15 and Figure 16 illustrate the sensitivity analysis of the Smagorinsky, Vreman and WALE models regarding the vertical streamwise velocity and TKE respectively. Since the streamwise vertical velocity $\langle w \rangle / U$, is the most significant velocity field in this flow simulation, Figure 15 shows the effects of different SGS model constants. In Figure 15(a), $\langle w \rangle / U$ of LES-SM is shown where two different SGS constant $C_s = 0.2$ and $C_s = 0.3$ is used and no significant change in $\langle w \rangle / U$ magnitude for this model. Furthermore, Figure 15(b) displays the effect of $C_v = 0.1$ and $C_v = 0.225$ in Vreman SGS model where little velocity fluctuation is observed. Figure 15(c) displays sensitivity of WALE model on changing model constant $C_w = 0.6$ to $C_w = 0.7$ where $\approx (2 - 3)\%$ deference ratio is seen at the near wall region. This change of the velocity field can be justified by the wall adaptive characteristics of the WALE model as the model is well adjusted with the model constant. On the contrary, other two SGS model performs as a stable sub-grid model for finding almost identical velocity fields on change of SGS

model constant.

Figure 16(a)-(c) depicted the further proofs of sensitivity of the model constants of different SGS models. Turbulent kinetic energy refers to the energy dissipation due to the modeling of small-scale effects of the flow regime. In Figure 16(b), $\approx 4.78\%$ increment of TKE is seen for LES-VM when the SGS constant is changed from $C_v = 0.1$ to $C_v = 0.225$ and $\approx 5.98\%$ change in TKE magnitude is found for LES-WM that is shown in Figure 16(c). On the other hand, LES-SM model has almost no effect on changing SGS model constant in the case of TKE. It is clear in the figures that, LES-SM is more stable SGS model than the other well-known sub-grid scale models Vreman and WALE.

4.8. Contribution of the SGS models

To simulate the turbulent flow the contribution of the different SGS models has been evaluated in terms of the SGS eddy kinematic viscosity $\nu_{sgs}(\bar{x}, t)$ normalized by the constant kinematic viscosity ν, that is shown in Figure 17 while $C_s = 0.2$, $C_v \approx 2.5C_s^2 = 0.1$ and $C_w = 0.6$ and $Re = 5000$. From this figure it is sen that the contribution is very larger from the Smagorinsky SGS model than the other two models. The Vreman model contributes significantly small and maximum turbulent flow features resolved numerically. Here it should be mentioned that for the present simulation to run LES with Vreman model it is mandatory to use minimum Smagorinsky constant $C_s = 0.2$ to correspond Vreman constant $C_v = 0.1$. For $Re = 5000$, if we take $C_v < 0.1$ the LES code is unstable numerically.

5. Conclusion

Airflow patterns inside indoor geometries determine the good healthy indoor environment. The airflow parameters vastly depend on the flow characteristics of turbulent behaviors. The better recirculation of the air all over the geometry ensures the good air quality inside the room. The turbulent intensities at different regions create recirculation zones inside the geometry by generating large and small-scale effects of the airflow. LBM is a powerful tool of the parallel computational framework for capturing turbulence of indoor airflow. To remedy the numerical instability of LBM at higher Reynolds number, LES can be used with LBM method to achieve a stable numerical simulation. Different sub-grid scale models can be used for modeling small-scale effects of turbulent flow structures in LBM-LES framework. Three different sub-grid scale model Smagorinsky, Vreman and WALE models are implemented in this present investigation.

In this present study, our initial objective was to achieve turbulent flow simulation inside a room using different SGS model in LBM-LES framework via state-of-the-art parallel programming in GPU. In evident, we validated our GPU based LBM CUDA code with well-known benchmark problems and conducted a grid independence test for the reliability of our simulation. In our present work, we tried to focus on the comparisons of turbulent behaviors inside an indoor environment for three different SGS models based on LBM framework. Furthermore, we extended our investigation on the effect of various SGS models for the two different model constants. In the case of evaluating the impact of SGS model, we found some difference in the simulating results where LES-VM model has larger turbulent intensities in lower sub-grid scale contribution rather than LES-SM and LES-WM simulation. But LES-SM showed excellent stability in flow simulation between the SGS models even if the model constant is changed. LES-WM produced numerical results for capturing turbulence with the consideration of no turbulence at the wall although little change in energy dissipation is seen due to shifting in the model constant in LES-WM. After discussing the case studies, we can conclude that the WALE model proves its wall adaptive behavior during the flow simulation. For all three model, most of the high turbulence occurs in the region below the inlet although the flow reached all over the indoor geometry and ventilated out through the outlet. Our work is implemented in context the of CUDA C programming platform which enables us to achieve a significant amount

of performance improvement than the traditional CPU computing. In a nutshell, better turbulent details are achieved in LBM-LES-Vreman and LBM-LES-WALE model rather than the classical LBM-LES-Smagorinsky model.

There is no enough research on different SGS model in the LES-LBM for simulating turbulent flows. So there is much room for implementing more advanced SGS model in LES with LBM framework like Dynamic SGS model to correct the airflow patterns for simulating the real scenario of airflow inside a room.

Acknowledgements

The second author gratefully acknowledges NVIDIA Corporation for granting the Tesla k40 GPU.

Funding

This research is conducted by the financial support of North South University (NSU) Faculty Research Grant "CTRG Grant No.:CTRG19/SEPS/09".

References

[1] H. Xing, A. Hatton, H. Awbi, A study of the air quality in the breathing zone in a room with displacement ventilation, Building and Environment 36 (7) (2001) 809–820.

[2] E. Mundt, Non-buoyant pollutant sources and particles in displacement ventilation, Building and Environment 36 (7) (2001) 829–836.

[3] T. Karimipanah, H. Awbi, Theoretical and experimental investigation of impinging jet ventilation and comparison with wall displacement ventilation, Building and Environment 37 (12) (2002) 1329–1342.

[4] X. Shao, X. Li, Evaluating the potential of airflow patterns to maintain a non-uniform indoor environment, Renewable Energy 73 (2015) 99–108.

[5] A. K. Melikov, Personalized ventilation, Indoor Air 14 (s7) (2004) 157–167.

[6] J. Kaczmarczyk, A. Melikov, P. O. Fanger, Human response to personalized ventilation and mixing ventilation, Indoor Air 14 (s8) (2004) 17–29.

[7] F. Rey, E. Velasco, Experimental study of indoor air quality, energy saving and analysis of ventilation norms in climatised areas, Energy and Buildings 33 (1) (2000) 57–67.

[8] J. Jiang, X. Wang, Large eddy simulation of airflows in a full scale room at different ventilation rates., ASHRAE Transactions 115 (2) (2009) 850–865.

[9] M. Wang, C.-H. Lin, Q. Chen, Advanced turbulence models for predicting particle transport in enclosed environments, Building and Environment 47 (2012) 40–49.

[10] Z. Zhang, Q. Chen, Comparison of the Eulerian and Lagrangian methods for predicting particle transport in enclosed spaces, Atmospheric Environment 41 (25) (2007) 5236–5248.

[11] B. Zhao, Y. Zhang, X. Li, X. Yang, D. Huang, Comparison of indoor aerosol particle concentration and deposition in different ventilated rooms by numerical method, Building and Environment 39 (1) (2004) 1–8.

[12] R. Przekop, A. Moskal, L. Gradoń, Lattice-Boltzmann approach for description of the structure of deposited particulate matter in fibrous filters, Journal of Aerosol Science 34 (2) (2003) 133–147.

[13] S. Jafari, M. Salmanzadeh, M. Rahnama, G. Ahmadi, Investigation of particle dispersion and deposition in a channel with a square cylinder obstruction using the lattice Boltzmann method, Journal of Aerosol Science 41 (2) (2010) 198–206.

[14] M. F. Hasan, T. A. Himika, M. M. Molla, Lattice Boltzmann Simulation of Airflow and Heat Transfer in a Model Ward of a Hospital, Journal of Thermal Science and Engineering Applications 9 (1) (2017) 011011.

[15] Z. Tian, J. Tu, G. Yeoh, CFD studies of indoor airflow and contaminant particle transportation, Particulate Science and Technology 25 (6) (2007) 555–570.

[16] T. Seta, E. Takegoshi, K. Okui, Lattice Boltzmann simulation of natural convection in porous media, Mathematics and Computers in Simulation 72 (2) (2006) 195–200.

[17] A. Mohamad, A. Kuzmin, A critical evaluation of force term in lattice Boltzmann method, natural convection problem, International Journal of Heat and Mass Transfer 53 (5) (2010) 990–996.

[18] A. Keating, P. Dethioux, R. Satti, S. Noelting, J. Louis, T. Van de Ven, R. Vieito, Computational aeroacoustics validation and analysis of a nose landing gear, in: 15th AIAA/CEAS Aeroacoustics Conference (30th AIAA aeroacoustics conference), 2009, p. 3154.

[19] T. Lee, C.-L. Lin, A stable discretization of the Lattice Boltzmann equation for simulation of incompressible two-phase flows at high density ratio, Journal of Computational Physics 206 (1) (2005) 16–47.

[20] K. Kono, T. Ishizuka, H. Tsuda, A. Kurosawa, Application of Lattice Boltzmann model to multiphase flows with phase transition, Computer Physics Communications 129 (1-3) (2000) 110–120.

[21] H. Huang, M. Sukop, X. Lu, Multiphase Lattice Boltzmann methods: Theory and application , John Wiley & Sons, 2015.

[22] U. Frisch, B. Hasslacher, Y. Pomeau, Lattice-gas automata for the Navier-Stokes equation, Physical Review Letters 56 (14) (1986) 1505.

[23] Y. Qian, D. d'Humières, P. Lallemand, Lattice BGK models for Navier-Stokes equation, Europhysics Letters 17 (6) (1992) 479.

[24] D. Rothman, S. Zaleski, Lattice Gas Automata (1997).

[25] D. A. Wolf-Gladrow, Lattice-gas cellular automata and lattice Boltzmann models: an introduction, Springer, 2004.

[26] H. Si, Y. Shi, Study on lattice Boltzmann method/large eddy simulation and its application at high Reynolds number flow, Advances in Mechanical Engineering 7 (3) (2015) 1687814015573829.

[27] S. B. Pope, Turbulent flows (2001).

[28] T.-H. Shih, W. W. Liou, A. Shabbir, Z. Yang, J. Zhu, A new k-ϵ eddy viscosity model for high reynolds number turbulent flows, Computers & Fluids 24 (3) (1995) 227–238.

[29] V. Yakhot, S. A. Orszag, Renormalization group analysis of turbulence. I. Basic theory, Journal of Scientific Computing 1 (1) (1986) 3–51.

[30] S. Kubacki, E. Dick, Simulation of plane impinging jets with k-ω based hybrid RANS/LES models, International Journal of Heat and Fluid Flow 31 (5) (2010) 862–878.

[31] D. Lakehal, W. Rodi, Calculation of the flow past a surface-mounted cube with two-layer turbulence models, Journal of Wind Engineering and Industrial Aerodynamics 67 (1997) 65–78.

[32] C. Meneveau, J. Katz, Scale-invariance and turbulence models for large-eddy simulation, Annual Review of Fluid Mechanics 32 (1) (2000) 1–32.

[33] W. Zhang, Q. Chen, Large eddy simulation of indoor airflow with a filtered dynamic subgrid scale model, International Journal of Heat and Mass Transfer 43 (17) (2000) 3219–3231.

[34] X. Cheng, F. Hu, Q. Zeng, Simulation of wind gust structure in the atmospheric boundary layer with lattice Boltzmann method, Chinese Science Bulletin 57 (10) (2012) 1196–1203.

[35] H. Yu, L.-S. Luo, S. S. Girimaji, LES of turbulent square jet flow using an MRT lattice Boltzmann model, Computers & Fluids 35 (8) (2006) 957–965.

[36] M. Fernandino, K. Beronov, T. Ytrehus, Large eddy simulation of turbulent open duct flow using a lattice Boltzmann approach, Mathematics and Computers in Simulation 79 (5) (2009) 1520–1526.

[37] H. Guan, C. Wu, Large-eddy simulations of turbulent flows with lattice Boltzmann dynamics and dynamical system sub-grid models, Science in China Series E: Technological Sciences 52 (3) (2009) 670–679.

[38] J. Smagorinsky, General circulation experiments with the primitive equations: I. The basic experiment, Monthly Weather Review 91 (3) (1963) 99–164.

[39] A. Vreman, An eddy-viscosity subgrid-scale model for turbulent shear flow: Algebraic theory and applications, Physics of Fluids 16 (10) (2004) 3670–3681.

[40] R. K. Moghadam, K. Javadi, F. Kiani, Assessment of the LES-WALE and Zonal-DES Turbulence Models in Simulation of the Flow Structures around the Finite Circular Cylinder., Journal of Applied Fluid Mechanics 9 (2).

[41] F. Nicoud, F. Ducros, Subgrid-scale stress modelling based on the square of the velocity gradient tensor, Flow, Turbulence and Combustion 62 (3) (1999) 183–200.

[42] M. Germano, U. Piomelli, P. Moin, W. H. Cabot, A dynamic subgrid-scale eddy viscosity model, Physics of Fluids A: Fluid Dynamics 3 (7) (1991) 1760–1765.

[43] D. K. Lilly, A proposed modification of the Germano subgrid-scale closure method, Physics of Fluids A: Fluid Dynamics 4 (3) (1992) 633–635.

[44] S. J. Emmerich, K. B. McGrattan, S. Kato, A. Baker, Application of a large eddy simulation model to study room airflow, Ashrae Transactions 104 (1998) 1128.

[45] H. Sajjadi, M. Salmanzadeh, G. Ahmadi, S. Jafari, Simulations of indoor airflow and particle dispersion and deposition by the lattice Boltzmann method using LES and RANS approaches, Building and Environment 102 (2016) 1–12.

[46] M. Wang, Q. Chen, On a hybrid rans/les approach for indoor airflow modeling (rp-1271), HVAC &R Research 16 (6) (2010) 731–747.

[47] D. d'Humières, Multiple–relaxation–time lattice Boltzmann models in three dimensions, Philosophical Transactions of the Royal Society of London A: Mathematical, Physical and Engineering Sciences 360 (1792) (2002) 437–451.

[48] S. Geller, M. Krafczyk, J. Tölke, S. Turek, J. Hron, Benchmark computations based on lattice-Boltzmann, finite element and finite volume methods for laminar flows, Computers & Fluids 35 (8) (2006) 888–897.

[49] A. G. Yiotis, J. Psihogios, M. E. Kainourgiakis, A. Papaioannou, A. K. Stubos, A lattice Boltzmann study of viscous coupling effects in immiscible two-phase flow in porous media, Colloids and Surfaces A: Physicochemical and Engineering Aspects 300 (1) (2007) 35–49.

[50] M. Bernaschi, M. Fatica, S. Melchionna, S. Succi, E. Kaxiras, A flexible high-performance lattice Boltzmann GPU code for the simulations of fluid flows in complex geometries, Concurrency and Computation: Practice and Experience 22 (1) (2010) 1–14.

[51] P. Bailey, J. Myre, S. D. Walsh, D. J. Lilja, M. O. Saar, Accelerating lattice Boltzmann fluid flow simulations using graphics processors, in: Parallel Processing, 2009. ICPP'09. International Conference on, IEEE, 2009, pp. 550–557.

[52] N. Delbosc, J. L. Summers, A. Khan, N. Kapur, C. J. Noakes, Optimized implementation of the lattice Boltzmann Method on a graphics processing unit towards real-time fluid simulation, Computers & Mathematics with Applications 67 (2) (2014) 462–475.

[53] C. Obrecht, F. Kuznik, B. Tourancheau, J.-J. Roux, A new approach to the lattice Boltzmann method for graphics processing units, Computers & Mathematics with Applications 61 (12) (2011) 3628–3638.

[54] M. M. Molla, B.-C. Wang, D. C. Kuhn, Numerical study of pulsatile channel flows undergoing transition triggered by a modelled stenosis, Physics of Fluids 24 (12) (2012) 121901.

[55] Q. Li, C. Zhong, K. Li, G. Zhang, X. Lu, Q. Zhang, K. Zhao, X. Chu, A parallel lattice Boltzmann method for large eddy simulation on multiple GPUs, Computing 96 (6) (2014) 479–501.

[56] Y. Kuwata, K. Suga, Imbalance-correction grid-refinement method for lattice Boltzmann flow simulations, Journal of Computational Physics 311 (2016) 348–362.

[57] A. J. Ladd, Numerical simulations of particulate suspensions via a discretized Boltzmann equation. Part 1. Theoretical foundation, J. Fluid Mech. 271 (1994) 285–309.

[58] M. J. Mawson, A. J. Revell, Memory transfer optimization for a lattice Boltzmann solver on Kepler architecture nVidia GPUs, Computer Physics Communications 185 (10) (2014) 2566–2574.

[59] J. Posner, C. Buchanan, Dunn-Rankin, Measurement and prediction of indoor air flow in a model room, Energy and Buildings 35 (5) (2003) 515–526.

[60] C. Shu, L. Wang, Y. Chew, Numerical computation of three-dimensional incompressible Navier-Stokes equations in primitive variable form by DQ method, International Journal for Numerical Methods in Fluids 43 (4) (2003) 345–368.

[61] H. C. Ku, R. S. Hirsh, T. D. Taylor, A pseudospectral method for solution of the three-dimensional incompressible Navier-Stokes equations, Journal of Computational Physics 70 (2) (1987) 439–462.

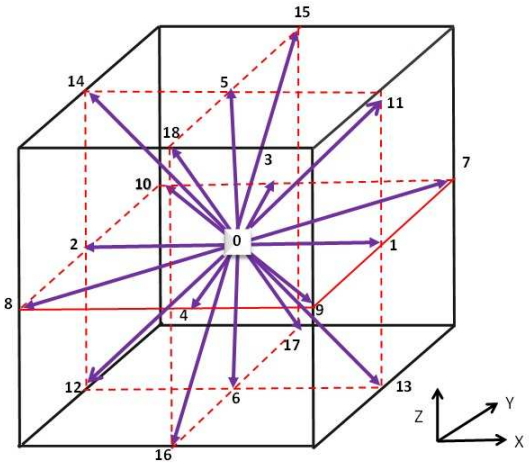

Figure 1: Lattice structure for the D3Q19 model.

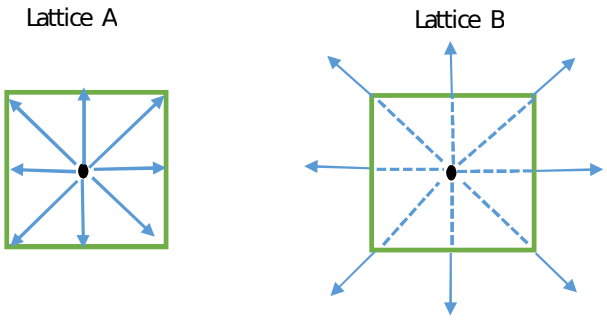

Figure 2: Pull-out scheme for LBM algorithm

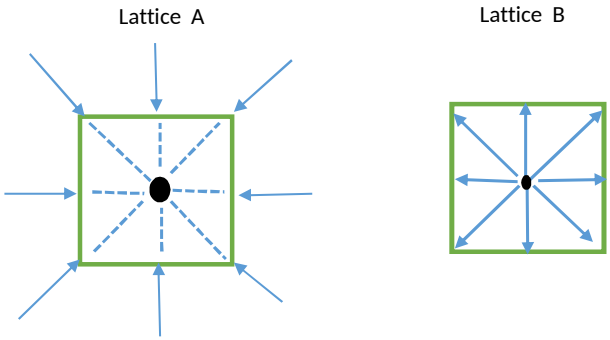

Figure 3: Pull-in scheme for LBM algorithm

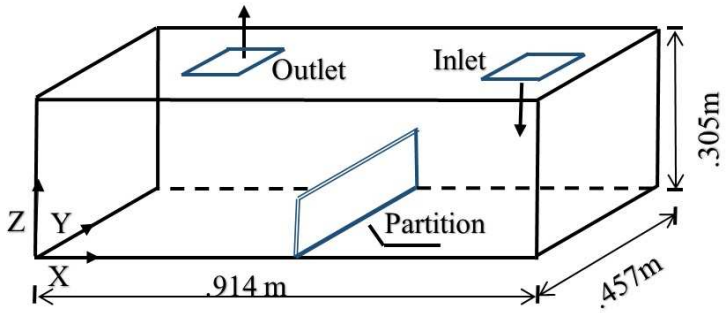

Figure 4: Physical geometry of the model room of [59]

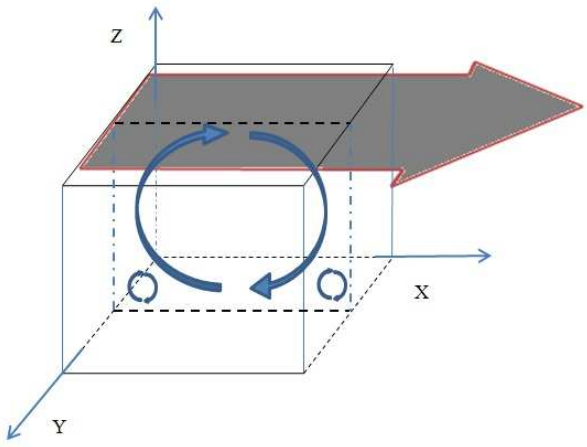

Figure 5: Schematic diagram of the cubic cavity

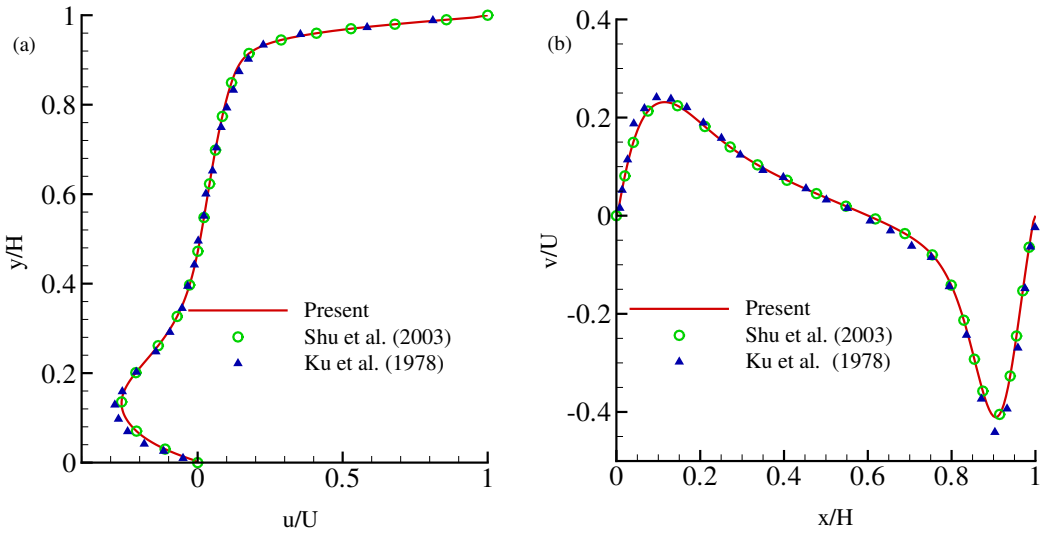

Figure 6: Comparison of the LBM results of lid-driven cubic cavity flow with the results of [60] and [61]: (a) u/U velocity at $x/H = z/H = 0.5$ (b) v/U velocity at $y/H = z/H = 0.5$ of the cubic cavity while $Re = 1000$ and without using any SGS model in LBM.

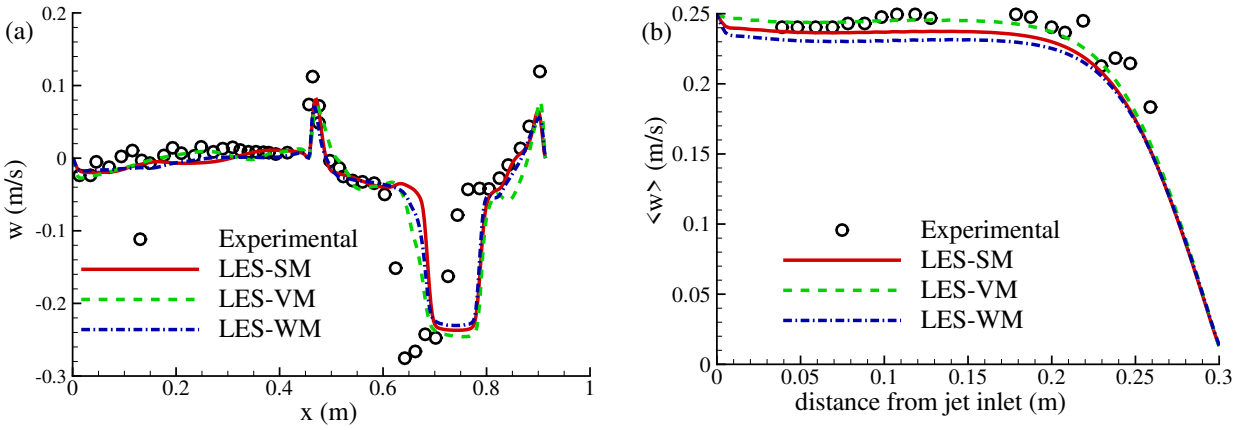

Figure 7: Comparison of the time-mean vertical velocity $\langle w \rangle$ with the experimental results of Posner [59] (a) above the partition at $z/H = 0.51$ and $y/H = 0.5$ and (b) along the vertical center line of the inlet at $x/H = 2.61$ and $y/H = 0.5$ while $Re = 1600$.

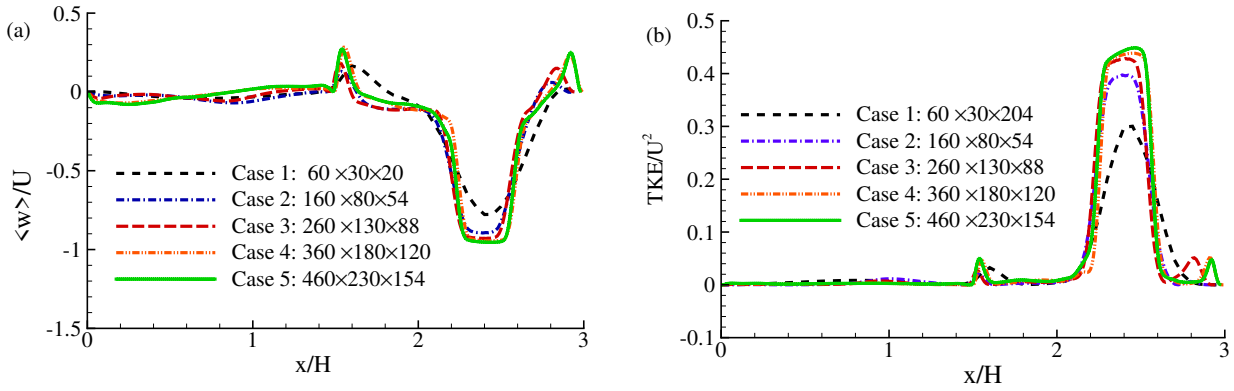

Figure 8: Grid Independence test of LBM-LES-SM results: (a) Mean streamwise velocity $\langle w \rangle / U$ and (b) turbulent kinetic energy $TKE \overset{\text{def}}{=} \frac{1}{2}\left(\langle u'^2 \rangle + \langle v'^2 \rangle + \langle w'^2 \rangle\right)$ for different grid sizes along the center line of x at $y/H = 0.5$ and $z/H = 0.51$ while $Re = 5000$.

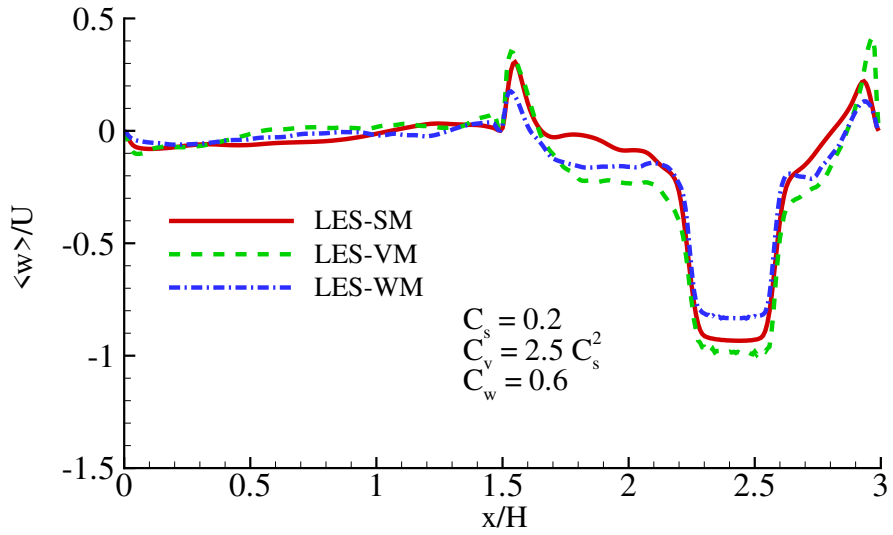

Figure 9: Time-mean vertical velocity $\langle w \rangle / U$ at $y/H = 0.50$ and $z/H = 0.51$ for three different SGS models while $Re = 5000$

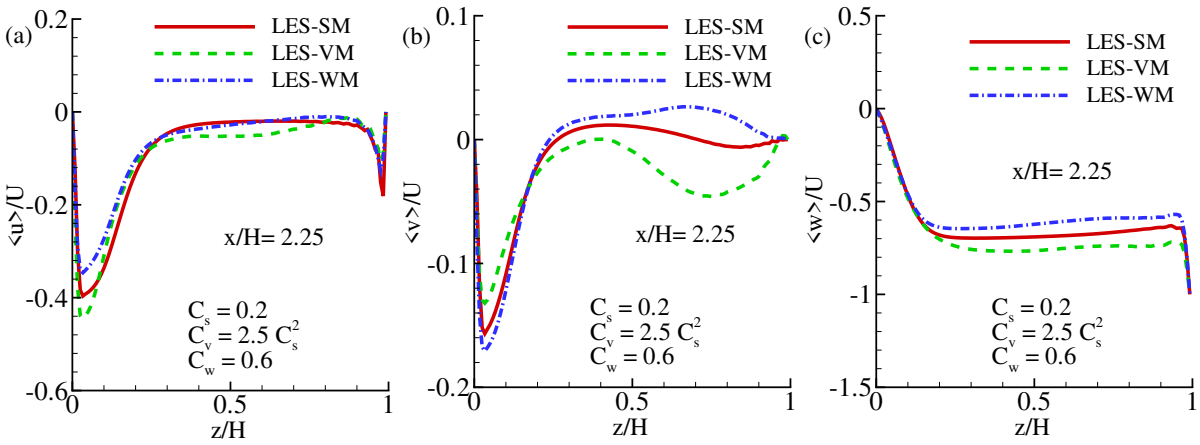

Figure 10: Time-mean velocity distribution for three different SGS models (a) $\langle u \rangle / U$ (b) $\langle v \rangle / U$ and (c) $\langle w \rangle / U$ at $y/H = 0.50$ and $x/H = 2.25$ while $Re = 5000$.

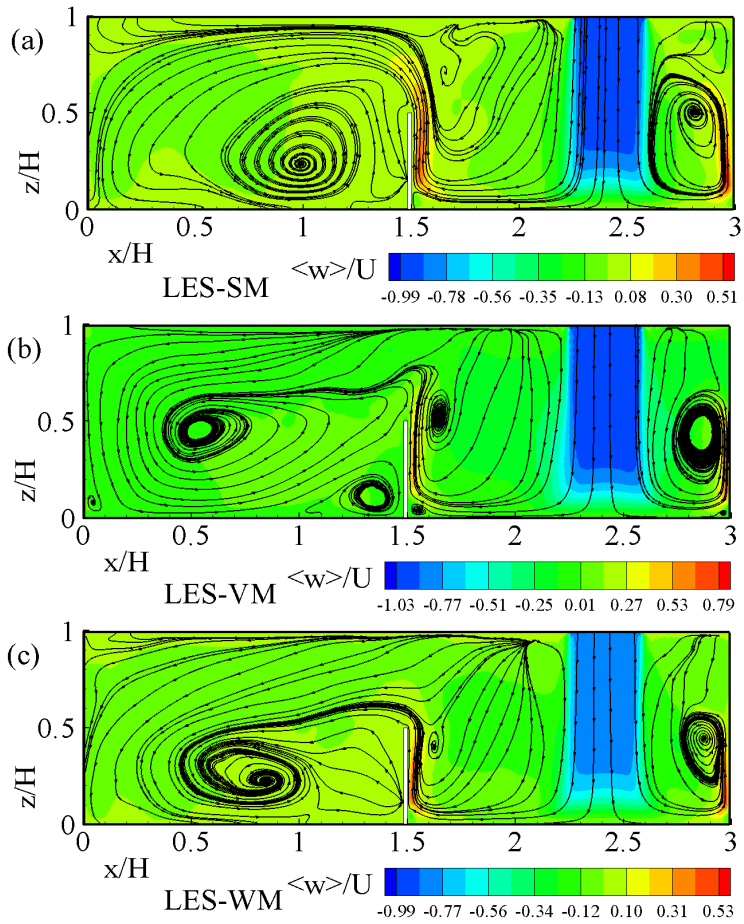

Figure 11: Stream wise mean velocity $\langle w \rangle$ contour in XZ-Plane of the geometry at Re=5000: (a).LBM-LES-Smagorinsky for $C_s = 0.20$, (b). LBM-LES-Vreman Model for $C_v = 0.10$, (c). LBM-LES-WALE Model for $C_w = 0.60$

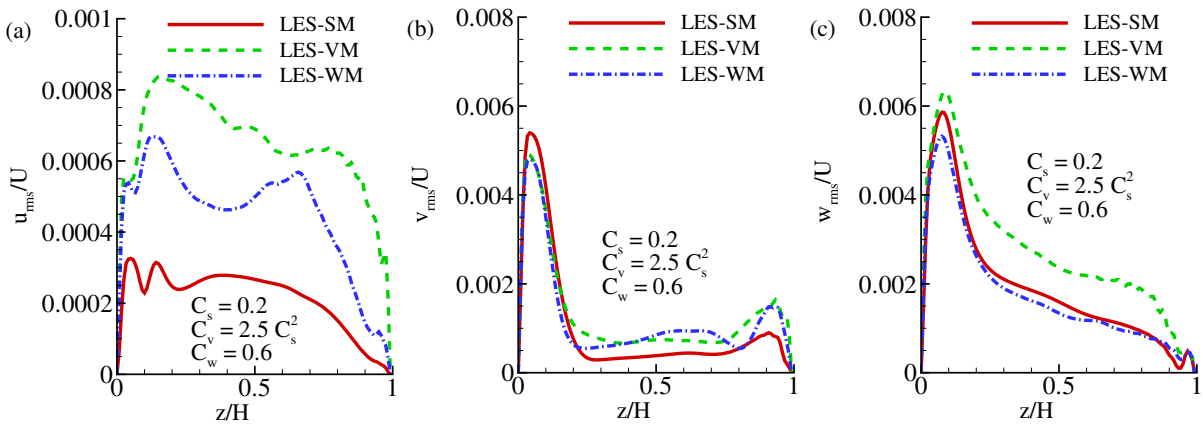

Figure 12: Root mean square velocity for three different SGS models (a) $u_{rms}/U = \sqrt{\langle u'^2 \rangle}/U$ (b) $v_{rms}/U = \sqrt{\langle v'^2 \rangle}/U$ and (c) $w_{rms}/U = \sqrt{\langle w'^2 \rangle}/U$ at $y/H = 0.50$ and $x/H = 2.61$ while $Re = 5000$.

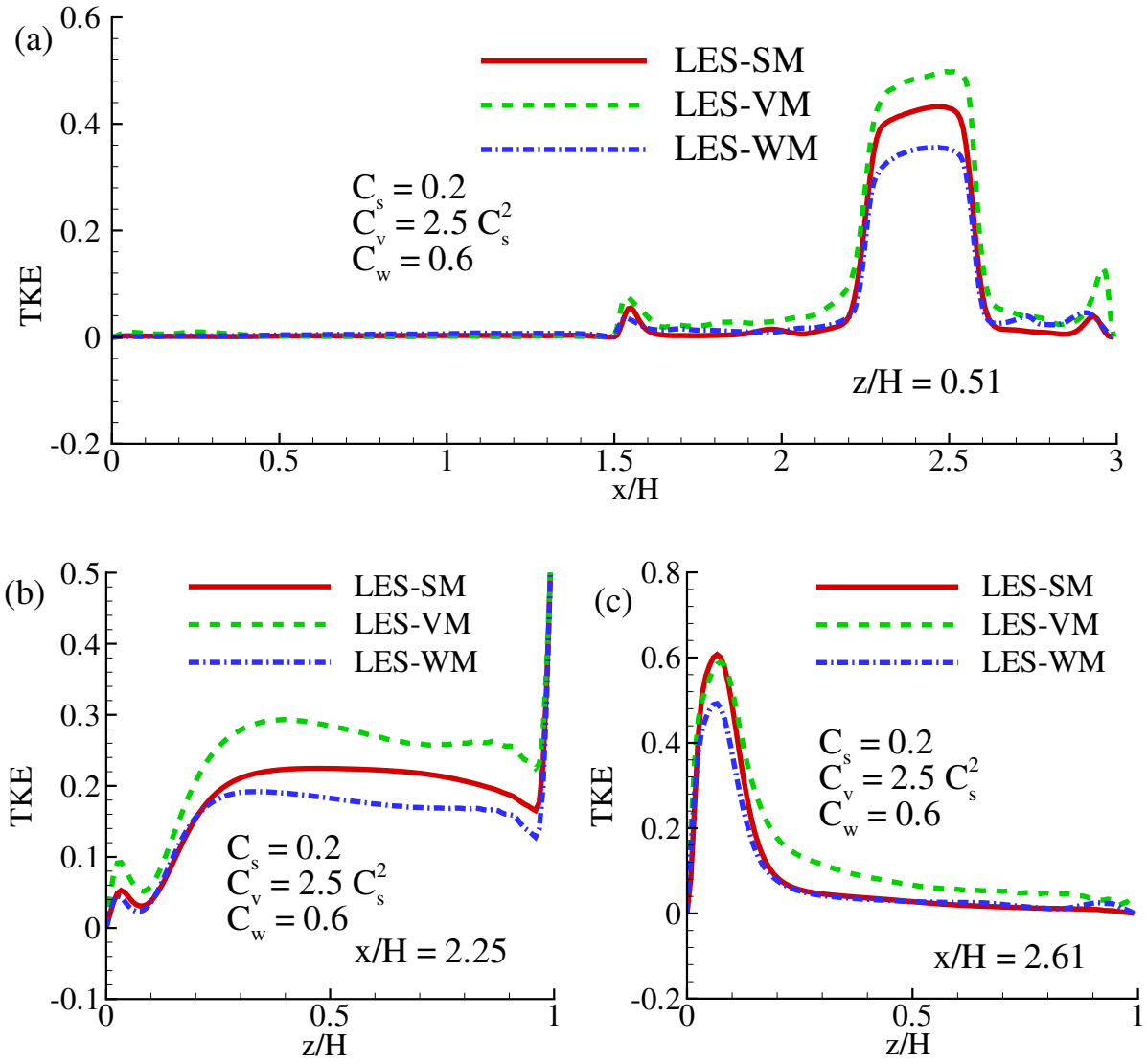

Figure 13: Normalized turbulent kinetic energy $TKE \overset{\text{def}}{=} \frac{1}{2}\left(\langle u'^2\rangle + \langle v'^2\rangle + \langle w'^2\rangle\right)/U^2$ for three different SGS models at (a) $y/H = 0.50$ and $z/H = 0.51$ (b) $y/H = 0.50$ and $x/H = 2.25$ (c) $y/H = 0.50$ and $z/H = 0.61$ while $Re = 5000$.

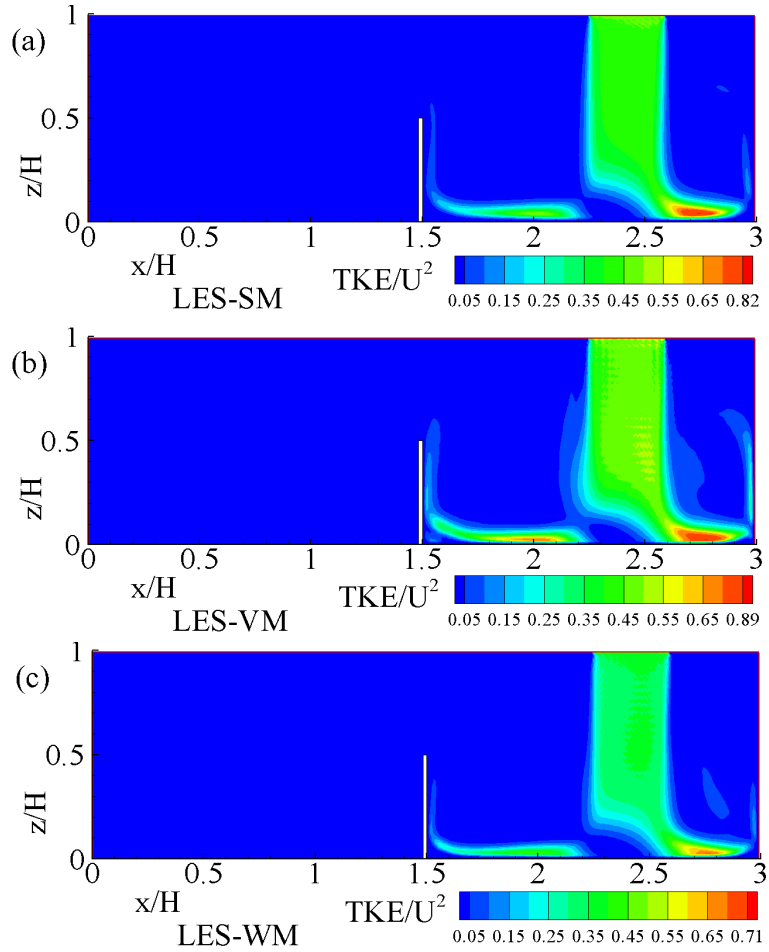

Figure 14: Contour plot of normalized turbulent kinetic energy $TKE \stackrel{\text{def}}{=} \frac{1}{2}\left(\langle u'^2\rangle + \langle v'^2\rangle + \langle w'^2\rangle\right)/U^2$ for three different SGS models (a) LES-SM (b) LES-VM (c) LES-WM while $Re = 5000$.

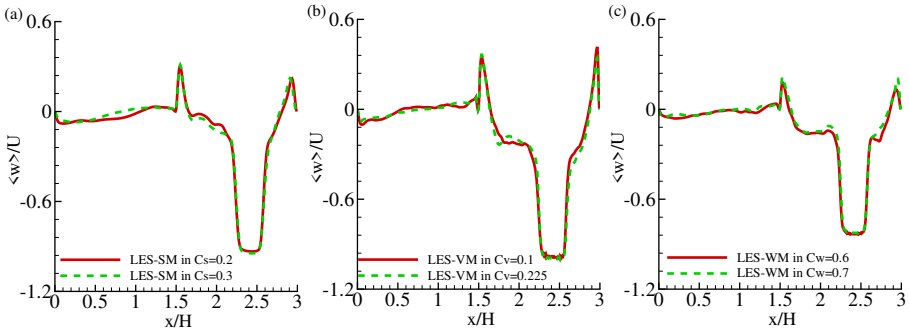

Figure 15: Vertical Mean velocity $\langle w \rangle / U$ at Re=5000 for (a) LES-SM in Cs=0.2 and 0.3 (b)LES-VM in Cv=0.1 and 0.225 and (c) LES-WM in Cw=0.6 and Cw=0.7

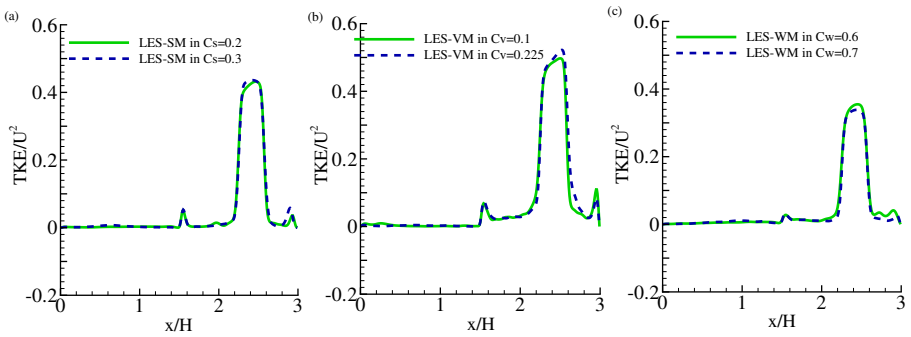

Figure 16: Effects of different SGS constants for TKE at Re=5000 for (a) LES-SM in Cs=0.2 and 0.3 (b)LES-VM in Cs=0.1 and 0.225 and (c) LES-WM in Cw=0.6 and Cw=0.7

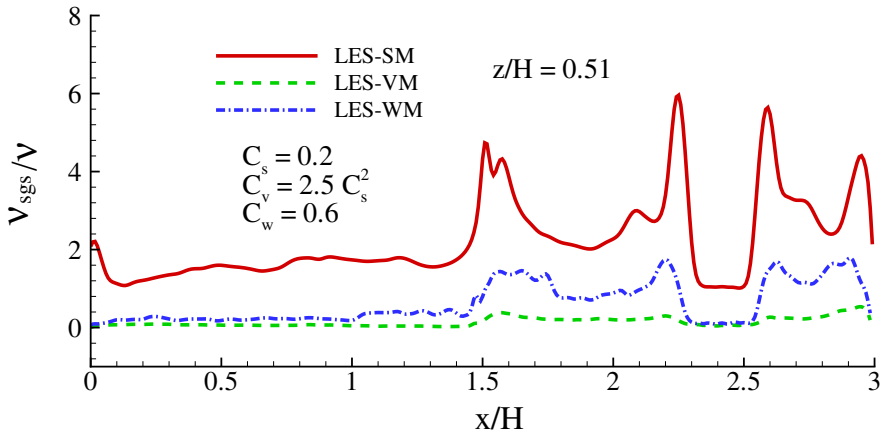

Figure 17: Normalized time mean SGS turbulent viscosity for the different SGS models while Re = 5000.